TÜBİTAK

Research Article

Utilizing resonant scattering signal characteristics via deep learning for improved classification of complex targets

Tuğçe TOPRAK[1,*]📷, **M. Alper SELVER**[2]📷, **Mustafa SEÇMEN**[3]📷, **E. Yeşim ZORAL**[2]📷
[1]The Graduate School of Natural and Applied Sciences, Dokuz Eylül University, İzmir, Turkey
[2]Department of Electrical and Electronics Engineering, Faculty of Engineering, Dokuz Eylül University,
İzmir, Turkey
[3]Department of Electrical and Electronics Engineering, Faculty of Engineering, Yaşar University, İzmir, Turkey

Abstract: Object classification using late-time resonant scattering electromagnetic signals is a significant problem found in different areas of application. Due to their unique properties, spherical objects play an essential role in this field both as a challenging target and a resource of analytical late-time resonant scattering electromagnetic signals. Although many studies focus on their detailed analysis, the challenges associated with target classification by resonant late-time resonant scattering electromagnetic signals from multilayer spheres have not been investigated in detail. Moreover, existing studies made the simplifying assumption that the objects having (one or more) layers constitute equal permeability values at the core and coatings. However, especially for metamaterials, magneto-dielectric inclusions require consideration of magnetic properties as well as dielectric ones. In this respect, this study shows that the utilization late-time resonant scattering electromagnetic signals of magnetic spheres provide diverse information and features, which result in superior object classification performance. For this purpose, first, time-domain late-time resonant scattering electromagnetic signals are generated numerically for single and multilayer radially symmetrical dielectric and magnetic spheres. Then, by using emerging deep learning tools, particularly convolutional neural networks trained with spheres having different material properties, a high multilayer object classification performance is achieved. Furthermore, by incorporating the frequency characteristics of the late-time resonant scattering electromagnetic signals to the classification process through Fourier transform and convolutional neural network layers for feature extraction, a convolutional neural network with long short term memory algorithm is developed. The outcome of the proposed algorithm design is shown to be particularly successful even in the case of limited available data on challenging targets. This extended strategy is also shown to outperform modern data augmentation and transfer learning techniques in terms of accuracy as well as the computational cost.

Key words: Target classification, scattered signals, transfer learning, long short-term memory, deep learning

1. Introduction

The importance of the scattering of electromagnetic radiation from a single sphere enables continuous research activities due to its emerging use in a broad range of applications, including but not limited to nanotechnology [1], meta-materials [2] and optics [3]. Despite its simple geometry, the sphere is a complicated target geometry due to its complex exterior and interior resonating modes, especially for late-time target recognition studies [4]. Accordingly, spherical objects are occasionally being used as a test-bed for new approaches [5].

Although detailed characteristics and analytical solutions supported by simulations are reported for many

---

*Correspondence: tugcetoprak.eee@gmail.com

334

cases and studies discussed in detail at Section 2 (i.e. Related work), up to our knowledge, there exists no study so far dealing with object identification or classification by using the scattered signals from multilayered spherical targets containing magnetic materials. Existing literature on object classification mostly made the simplifying assumptions that the permeability remains the same throughout the core and coating layers. However, especially for meta-material production, magneto-dielectric inclusions play an essential role, and therefore the analysis of magnetic properties gains higher value both in theory and practice [6].

In the last decade, there has been outstanding accomplishments on target classification performance using machine learning due to the advancement of deep learning strategies. Deep models have achieved state-of-the-art results in various fields including but not limited to medical imaging [7], industrial image processing [8], transportation [9–11], and other diverse applications of signal and information processing [12]. However, as discussed in the next section, they have limited applications in target recognition from 1-D signals.

In this study, first, single and multilayer spherical targets having varying dielectric and magnetic properties are modeled, and their LARSESs are generated. Newly produced LARSESs for multilayer magnetic spheres complement those provided by dielectric ones enabling extended diverse features. It is shown that superior multilayer object classification is achieved through the proposed CNN based strategy utilizing these diverse features. Finally, the proposed classification strategy is extended to measured signals through data augmentation and transfer learning (TL) techniques. The results show that LARSESs of magnetic spheres also provide improved performance for more complex targets such as aircraft models. Furthermore, as a second contribution, CNN-LSTM approach is developed to overcome the need for the vast number of initial training data, optimistic bias (i.e. peeking), and high operational cost due to multiple model usage.

It is observed that the training of LSTMs by using a small amount of LARSESs of real targets requires improved feature extraction for better classification. Accordingly, the frequency components of LARSESs are incorporated via Fourier transform, and the distinctive features of LARSESs are revealed. Finally, CNN-LSTM algorithm is trained with this extended feature set, and the results show that the application of proposed CNN-LSTM architecture provides improved complex target classification performance without the shortcomings mentioned above.

The rest of the paper is organized as follows: In Section 2 the related work is presented. Section 3 introduces the generated scattering fields for data sets. The existing systems and their limitations are given in Section 4. Section 5 describes the developed strategy. The application results are given in Section 6. Overall evaluations and discussions are presented in the conclusion section.

2. Related work

Analysis of linearly polarized scattered electromagnetic plane waves from a homogeneous conductor or dielectric sphere has been studied extensively [4]. Moreover, the utilization of those scattered signals is shown to be effective on the classification of spherical targets even under low signal-to-noise ratio (SNR) conditions [13]. On the other hand, the analysis of multilayered spheres in terms of obtaining computational forms for their scattered fields has recently been discussed in detail [6]. When the scattering from spherical targets is extended to multilayered conditions, the variety of possibilities motivated further research studies on obtaining solutions for more challenging cases such as uniaxial dielectric spheres [14], radially [15] and/or rotationally symmetric inhomogeneous anisotropic spheres [16].

Besides the advancements on the material side, new object classification strategies, namely convolutional neural networks (CNNs) have achieved great improvements. Being a member of the deep learning (DL)

framework [17] they have been frequently used in 2-D electromagnetic tasks, which are dominated by synthetic aperture radar (SAR) image classification [18]. However, they have limited applications in 1-D such as range profiles [19], raw radar echoes [20], and time-frequency representations [21]. A recent application of CNN to late-time resonant scattered electromagnetic signals (LARSESs) show their promising potential under correct parameterization and architecture, but it is limited to dielectric objects [22].

Long short-term memory (LSTM) algorithms are effective tools when training with a sequence is the matter. They are more feasible than CNNs in 1-D applications. In this respect, the high performance of LSTMs in 1-D classification problems has been demonstrated in radar applications such as; target classification with backscattering electromagnetic signals [23], automatic target recognition with radar cross-section [24] and SAR [25]. Even though LSTMs have high performances, some applications require extended feature extraction to represent targets in a better way [25]. In this regard, feature extraction for LSTM with convolution layers is a new approach that combines CNNs and LSTMs (CNN-LSTM).

3. Generation of training and test LARSES sets

In this study, the performance of the object classification system is improved when targets with magnetic materials are used for the training of CNNs. For this purpose, three target sets, which are in resonance (or Mie) scattering region, are considered. Here, while the first target set is processed for initial training of deep learning transfer in CNNs, the second and the third sets are used for both transfer learning and test sets through cross-validation. Besides, to increase the flexibility and variety in the extraction of scattered fields, the fields of the first target set are obtained by using analytical expressions, which enables several synthesized signals for the training of CNNs to give better performance. On the other hand, the targets in second and third sets include a low number of simulation and measurement scattered fields, respectively, to show that the proposed method works well even the scattered signals of the test targets are with a limited number. Some of the spherical targets in the first and second sets contain magnetic materials, and aircraft models used in the third set include some magnetic materials such as iron or iron alloy. The details of the computational setup (Figure 1a), simulation (Figure 1b), measurement setup (Figure 1c), train/target sets, and their properties are explained in detail as follows.

3.1. Target set 1: magnetic/dielectric single layer spheres

Penetrable (dielectric, and magnetic) spheres are useful and challenging target geometries for classification methods. Despite their simple geometry, the scattering mechanism from these objects are complex due to many exterior and interior resonant modes (poles). On the other hand, the scattered field signals from these objects can be analytically calculated in the frequency domain for a uniform plane wave excitation at any aspect angle and polarization by using Mie expressions/formulas [4, 26]. For the geometry shown in Figure 1a, which is considered for the extraction of scattered fields of the uniform single layer spheres, the scattered far fields are equated as [26];

$$E_\theta^s \simeq jE_0 \frac{e^{-jk_0r}}{k_0r} \cos\phi \sum_{n=1}^{\infty} j^n \left[b_n \sin\theta P_n^{'1}(\cos\theta) - c_n \frac{P_n^1(\cos\theta)}{\sin\theta} \right] \tag{1}$$

$$E_\phi^s \simeq jE_0 \frac{e^{-jk_0 r}}{k_0 r} \sin\phi \sum_{n=1}^{\infty} j^n \left[b_n \frac{P_n^1(\cos\theta)}{\sin\theta} - c_n \sin\theta P_n^{'1}(\cos\theta) \right], \tag{2}$$

where

$$b_n = \frac{\epsilon_r j_n(Nk_0 a) \left[x j_n(x) \right]'_{k_0 a} - j_n(k_0 a) \left[x j_n(x) \right]'_{Nk_0 a}}{\epsilon_r j_n(Nk_0 a) \left[x h_n^{(2)}(x) \right]'_{k_0 a} - h_n^{(2)}(k_0 a) \left[x j_n(x) \right]'_{Nk_0 a}} \tag{3}$$

$$c_n = \frac{\mu_r j_n(Nk_0 a) \left[x J_n(x) \right]'_{k_0 a} - j_n(k_0 a) \left[x j_n(x) \right]'_{Nk_0 a}}{\mu_r j_n(Nk_0 a) \left[x h_n^{(2)}(x) \right]'_{k_0 a} - h_n^{(2)}(k_0 a) \left[x j_n(x) \right]'_{Nk_0 a}}. \tag{4}$$

Here, $N = \sqrt{\epsilon_r \mu_r}$ is the index of refraction, $k_0 = 2\pi/\lambda_0$ is the free space wavenumber, and j_n, $h_n^{(2)}$ and P_n^1 represents spherical Bessel, spherical Henkel (second kind) and associated Legendre (first kind) functions, respectively. Finally, time-domain scattered fields can be obtained for any incident waveform (pulse) by using frequency-to-time domain conversion.
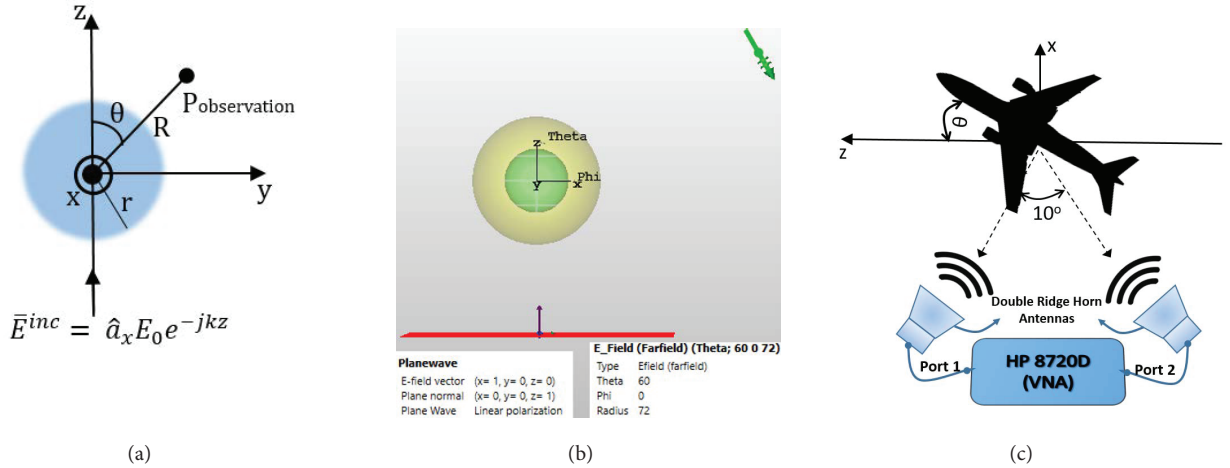

Figure 1. The (a) computational, (b) simulation/CST, and (c) measurement setup.

Here, all parameters of the setup except the constitutive material parameters (permittivity and permeability) of the spheres are kept constant for all single layer spheres taken into account. All spheres have radii of 1.8 cm, and their scattered field analytical responses are generated at the frequency range of 0–12 GHz with a frequency resolution of 10 MHz. By considering the dimensions of the spheres and frequency ranges, the targets can be considered in the resonance scattering region. The observation point is selected as $R = 72$ cm away from the center of the spheres, and ϕ-polarization (E_ϕ in Equation 1) bistatic responses are collected at $\phi = 90°$ plane (or yz plane) for several different θ values (from $0°$ to $179.9°$ with $0.1°$ resolution). Three dielectric spheres with relative permittivity values of $\epsilon_r = 2, 3, 4$ and constant relative permeability value of $\mu_r = 1$, and three magnetic spheres with relative permeability values of $\mu_r = 100, 200, 300$ and constant relative permittivity value of $\epsilon_r = 1$ are used in the first target set for the initial training. The relative permeability

values for magnetic spheres are selected high enough to be consistent with realistic magnetic materials such as nickel or magnetic iron. The frequency-domain responses are converted into time-domain responses by using a 1% lowpass Gaussian window and inverse fast Fourier transform (FFT) and zero padding in order to obtain signals with a time resolution of approximately 5 ps. All signals in this target set have 1500 time samples giving a total time duration of about 7.5 ns. The sample time-domain scattered signals for single layer dielectric spheres and magnetic spheres are demonstrated in Figures 2a and 2b, respectively.
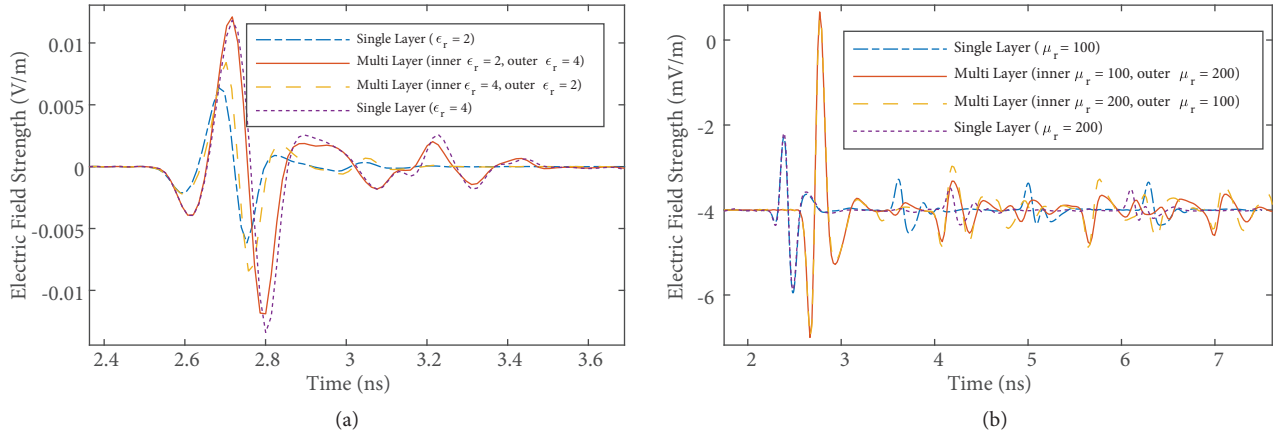

(a)

(b)

Figure 2. The time domain scattered signals at $\theta = 60^o$ illustrating different characteristics of four (a) dielectric spheres two having a single layer and two having multilayers, and (b) magnetic spheres two having single layer and two having multilayers. (The time-span between (a) and (b) is different for better illustration of amplitude variations above a certain threshold.)

3.2. Target set 2: magnetic/dielectric multilayer spheres

For the second target set, which is also the first "test" target set, multilayer penetrable spheres are utilized. Multilayer and buried dielectric spheres are studied in many works [6–16, 27, 28]; however, multilayer magnetic spheres are considered as targets for the first time in this study. Although Mie expressions can also be extended to get the frequency-domain responses of multilayer spheres, time-domain scattered fields are generated from the simulations carried out with CST Microwave Studio from which Figure 1b depicts the related configuration. Here, the setup for the generation of scattered fields for single layer spheres is desired to be discriminated from those for multilayer spheres as much as possible. For this purpose although the direction and polarization vector for incident plane-wave are the same with the ones in single spheres; incident wave in CST has different incident waveform (pulse) than the one used for the extraction of time-domain signals in Section 3.1. Thus, it is aimed to show that the proposed method shows satisfactory performance regardless of the waveform (pulse) impinging on targets.

Besides, the bistatic responses are obtained with an E-field probe oriented in θ direction for θ-polarized scattered fields at $\phi = 0°$ plane (or xz plane) in the frequency range of 0-8 GHz with 1 MHz frequency resolution, all of which are different from the ones given for the single spheres. Thus, it is also aimed to demonstrate that the method is insensitive to the changes in aspect angle, polarization and frequency band. Having a thickness of 0.9 cm for each two uniform layers, total radius of two-layer spheres is again taken as 1.8 cm. Two multilayer dielectric spheres (one has inner and outer relative permittivity values of $\epsilon_{r1} = 2$ and $\epsilon_{r2} = 4$, respectively, and the other has $\epsilon_{r1} = 4$ and $\epsilon_{r2} = 2$) and two multilayer magnetic (one has inner and outer relative permeability values of $\mu_{r1} = 100$ and $\mu_{r2} = 200$, respectively, and the other has $\mu_{r1} = 200$ and $\mu_{r2} = 100$.) are used for

this target set. The other relevant parameters set in CST simulations are: solver = time domain, mesh type = hexahedral, cells per wavelength = 25 (maximum cell both for near to model and far to model), minimum cell = 25 (fraction of maximum cell near to model), refinement around edge = 20 (fraction of maximum cell near to model), additional cell around edge = 20, boundary = open (add space) in all directions, settings for PML boundary = $\lambda_0/4$ @4GHz (automatic minimum distance to structure). LARSESs for these targets are gathered for fewer number of θ values of 0° to 180° with 5° resolution (where a sample case of $\theta = 60°$ is shown in Figure 1b) as compared to number of scattered fields for single layer spheres in Section 3.1 (Figure 3). All signals in this target set have total time duration of about 11.5 ns.
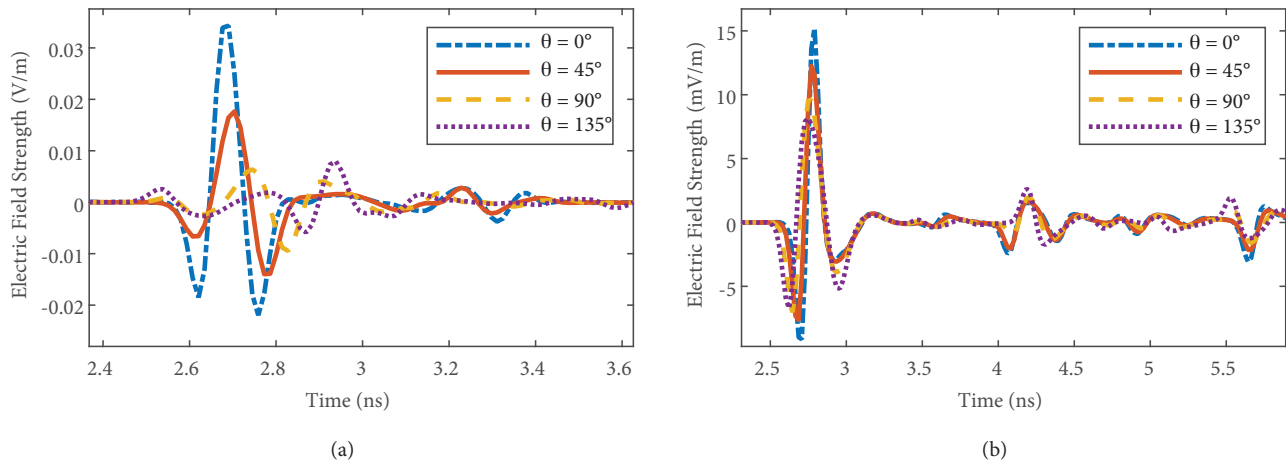

Figure 3. The scattered signals at different bistatic elevation angles from multilayered (a) dielectric sphere (inner layer with $\epsilon_{r1} = 2$, outer layer of $\epsilon_{r2} = 4$), and (b) magnetic sphere (inner layer $\mu_{r1} = 100$, outer layer $\mu_{r2} = 200$).

3.3. Target set 3: real targets–small-scale airplane models

The third target set contains three small-scale models of real airplanes, which are Boeing 747, Boeing 767, and DC-10. All targets are 1/500 scaled models such that the body, wing, and tail lengths are 14.5, 12.7, and 4.8 cm for Boeing 747; 12.48, 12.54, and 5 cm for Boeing 767; and 12.7, 11.4, and 5.25 cm for DC-10, respectively. The LARSESs of these targets are obtained with a measurement setup consisting of an HP8720D two-port vector network analyzer and two wideband (1-12 GHz) double-ridge horn antennas (Figure 1c). The centers of airplane models are 95 cm away from aperture centers of both antennas such that a small bistatic angle of 10 degrees is formed between target and horn antennas. Therefore, these measurements might be evaluated as almost monostatic scattered responses. VV polarization measurements are made in the frequency range of 1–12 GHz with 13.75 GHz resolution that the targets again fall into the resonance region. The frequency responses with Kaiser–Bessel frequency window implemented in network analyzer are measured for different angular positions of airplane models (from $\theta = 0°$ to $\theta = 180°$ with 10° resolution as shown in Figure 1c) by rotating them over H-plane [4]. Finally, time-domain signals, where sample measured scattered signals are given in Figure 4, are obtained with inverse FFT and zero padding with a time resolution of approximately 5 ps. All signals in this target set have 1024 time samples giving a total time duration of about 5.1 ns.
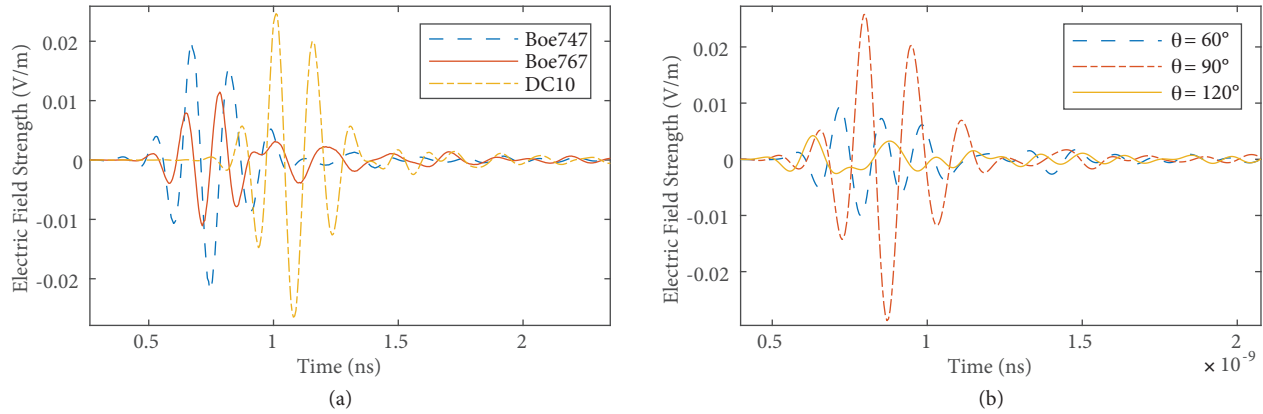
Figure 4. The measured scattered signals (a) from different type of small-scale aircraft models at $\theta = 100°$, and (b) from Boeing 747 model at different elevation angles.

4. Existing two-stage deep system employing data augmentation and transfer learning

This section provides an overview of the previous study [22], which uses simulated or analytic solutions of simple targets providing an excessive amount of scattered signals. The extensive number of data allows end-to-end training of deep models. Then, the last layers of these initially trained models are adapted to complex targets using transfer learning via measured signals. This approach was previously applied using only conductor and dielectric spheres as the base target set [22]. In this study, the approach has been extended with magnetic spheres, and it is shown to provide higher accuracy as well as complementary information, which can be used to obtain higher detection performance. The following subsection delivers the details of the abovementioned methodology.

4.1. Stage 1: generating CNN models using synthetic data

One of the very first implementation and application of 1-D CNNs is performed for electrocardiographic (ECG) data processing in [29], in which their foundations are given in detail. Based on those analyses, here, only the main design parameters of the utilized models are given without explicit representation of their formulation.

Stage 1 starts with preprocessing by normalization, which significantly increases stabilization (preventing divergence) and decreases the training time. Normalization enables the signals to have zero mean and unity standard deviation. Then, zero padding is applied to avoid size mismatch between scattered signals of different targets. The input layers are designed to receive complete normalized signals.

Convolutional layers of the CNNs include 16 filters, all of which have a 3-by-3 kernel size. They are followed by nonlinear activation functions chosen as rectified linear units. Padding is used to ensure the same size at the output and the input layers. Next, three fully connected layers (FCLs), which are connected to all the neurons in the preceding layers, are used. In this way, all the features learned by the previous layers to are combined to identify the larger patterns. The first two FCLs are designed to have 384 hidden neurons. The size of the last FCL is set to be equal to the number of targets (i.e. four for multilayer spheres and three for aircraft models).

The output of the FCL is normalized by the softmax activation function, which provides positive numbers that sum to one and is utilized to derive the output probabilities of the classification layer that uses the calculated probabilities to assign the input to one of the mutually exclusive target classes and computes the loss. Each

network is trained by stochastic gradient descent with momentum using an initial learning rate of 0.01 and mini-batch size as 128 for 20 maximum number of epochs.

4.2. Stage 2: fine-tuning the CNNs to real targets by TL

In stage 2, the generic models generated at stage 1 are adapted to the actual targets (multilayer spheres and aircraft models) by using TL applied to the last three layers (FCL, softmax, and classification), which are retrained using the small number of measured scattered signals [22]. The features extracted at the initial layers of generic CNN cover general resembling characteristics of the scattered signals (e.g., damping oscillations). Hence, the weights of the initial layers until the last FCL are used from pretrained CNN.

TL ensures a systematic approach to improving the reduced performance of the generic CNNs at the classification of real targets due to the mismatch between the training and the test sets. Thus, the lack of adaptation between elementary and real targets is compensated at this stage by taking advantage of the correlation between the LARSESs data sets. The effects of increasing training samples for TL are tested by various data augmentation techniques. After extensive experimentation and simulations, two techniques are employed: 1) Adding varying levels of Gaussian noise to the signals. Particularly, two SNR levels are used (i.e. 10 dB, 20 dB). 2) Scaling the scattered signal amplitudes by factors of 0.5, 0.9, 1.1, and 1.5.

4.3. Limitations and shortcomings of two-stage system

Although the abovementioned model generation strategy can provide improved target classification performance, it requires an ensemble of multiple models to achieve state-of-the-art results, as discussed in [22]. Such a strategy relies on the resemblance of the LARSESs between base target sets (i.e. spheres) and the actual targets (i.e. airplanes), which might not be available for all kinds of complex targets. In the lack of this resemblance, it might be difficult to construct a base target set having similar properties to the LARSESs of actual targets. Thus, a system that would only use the data of actual targets and process it from multiple perspectives can be more self-sufficient. Another critical shortcoming occurs due to combining multiple models with an ensemble when only limited data is available. The individual target classifiers (i.e. ensemble members) are already tested with measured data causing dependency between train and test data of the ensemble, a phenomenon referred to as "peeking" [20]. In other words, since the individual classifiers are already tuned to achieve high scores, the ensemble result might be optimistically biased. Last but not least, a major drawback is the operational cost of multiple deep models, which would require significant computational power to achieve desired real time performance. To overcome these limitations, a new system is developed and described in the following section.

5. Proposed CNN-LSTM system

5.1. Feature extraction by using Fourier transform

The significant problems of the target classification from scattered signals are the strong dependency of signals on the frequency, polarization, and aspect angles [30]. The measurement setup mentioned in the previous section is designed to overcome the difficulties originated from these dependencies. Although the design procedure is presented to achieve higher performance of classification, the amplitudes of LARSESs of the small-scale airplane models are measured very close to each other and small to be classified as can be seen from Figure 4. Even though this small amplitude problem can be handled by scaling, this is not preferred as a preprocessing technique since the scattered signals obtained from different airplanes have very similar characteristics at different angles. Thus,

the airplane classification process requires further feature extraction to represent LARSESs' characteristics in the best manner.

The feature extraction technique used in this study utilizes the Fourier transform (FT) to construct the LARSESs of small-scale airplane models in the frequency domain. FT decomposes a signal into its frequency components and enables overcoming the waveform similarity problems in the time domain. Even though signals from Boeing 747 at 90° and DC10 at 100°, and also signals from Boeing 747 at 60° and Boeing 767 at 100° have similar characteristics Figure 4, their frequency components are different from each other Figure 5. Hence, feature extraction by using FT commits better classification in comparison with raw or scaled data classification.
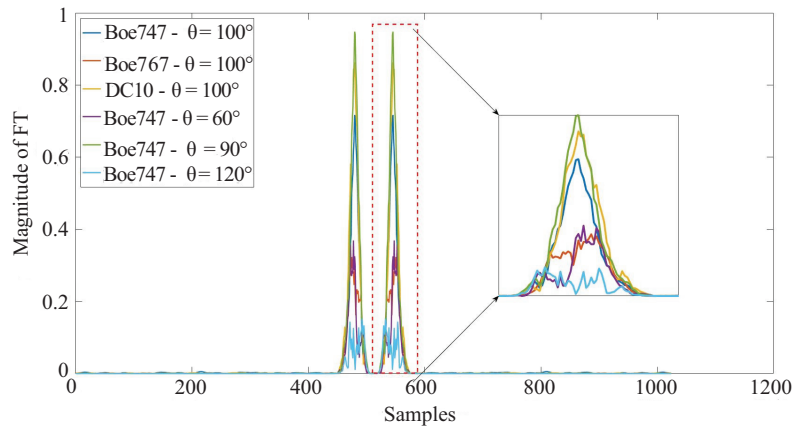

Figure 5. FTs of LARSESs in both Figures 4a and 4b.

5.2. CNN-LSTM algorithm for classification

Traditional CNN algorithms are generally designed for classification or detection from images since their convolutional layers are two dimensional. On the other hand, LSTM algorithms are appropriate for the classification of sequences. Hence, LARSESs are more suitable to be classified with LSTM algorithms. However, raw data or its extracted features might not provide enough information to achieve higher classification performance with LSTMs. At this step, the feature extraction process of convolutional layers on CNN can be embedded to LSTM algorithm. That modification makes LSTM to be trained with the output of convolutional layers Figure 6.
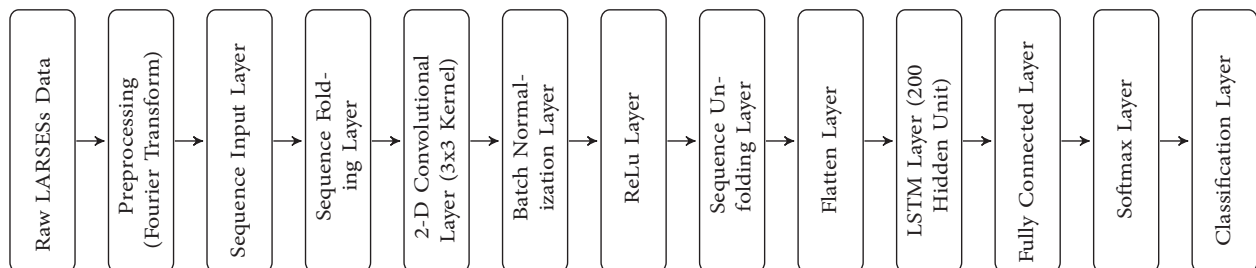

Figure 6. Layer scheme of CNN-LSTM algorithm.

The CNN part of the proposed hybrid algorithm includes convolutional, normalization and rectified linear unit (ReLu) layers. Convolutional layer has 16 channels which contain $3\times3\times1$ convolution kernel as given

in Table 1. The kernel connects to small part of input data from previous layer. The connection weights (i.e. convolutional kernel) of every channel in convolutional layer evolves with training. The output of the convolution layer will be an input of the ReLu to reduce the linearity, after the normalization. In this application, the convolutional layer reflects the spacial information of the input data as an output.

Table 1. Analysis of each layer of CNN-LSTM network given in Figure 7.

Name	Properties	Type	Activations	Learnables
input	Sequence input layer with 100×1×1 dimensions	Sequence input	1000×1×1	-
fold	Sequence folding	Sequence folding	Out 1000×1×1 Mini-batch size 1	-
conv	16 3×3×1 convolutions with stride [1 1] and padding 'same'	Convolution	1000×1×6	Weights 3×3×1×16 Bias 1×1×16
bn	Batch normalization with 16 channels	Batch normalization	1000×1×16	Offset 1×1×16 Scale 1×1×16
relu	ReLu	ReLu	1000×1×16	-
unfold	Sequence unfolding	Sequence unfolding	1000×1×16	-
flatten	Flatten	Flatten	16000	-
lstm	LSTM with 200 hidden units	LSTM	200	Input weights 800×16000 Recurrent weights 800×200 Bias 800×1
fc	3 fully connected layers	Fully connected	3	Weights 3×200 Bias 3×1
softmax	Softmax	Softmax	3	-
classification	Crossentropyex with '1' and 2 other classes	Classification output	-	-

LSTM is one of the most used recurrent neural networks (RNNs). The LSTM uses 4-gate mechanism selectively which passes/drops information from the sequential input data. The dependency of the elements in the sequence can be preserved with that mechanism. The LSTM have two sets of parameters, which are called the cell and hidden states. An element fed into the mechanism comes through the forget-gate first. The inputs of the forget-gate are the element of the sequence and previous hidden state. It gives a temporary output called as f_t, where t represents current state. The second one is input-gate, which takes same inputs as the forget-gate and gives two temporary variables: i_t and $\tilde{C}_t$. To update the current cell state, the previous cell state C_{t-1} and all temporary variables f_t, i_t and $\tilde{C}_t$ are fed into the updating gate. Finally, for calculating the current hidden state h_t, the output gate takes the previous hidden state h_{t-1}, the current element of sequence and the current cell state.

CNN-LSTM algorithms have two important layers that do not exist in traditional LSTMs and CNNs. One of them is called as "sequence folding layer" which is responsible for converting sequence input to the two-dimensional input of the convolutional layer. Inversely, the other one, "sequence unfolding layer" is responsible

for converting two-dimensional features to sequence input of LSTM layer.

The connection analysis of the trained CNN-LSTM network is given in Figure 7 and Table 1. Figure 7 clearly shows the layer connection difference of CNN-LSTM network with respect to traditional CNNs. Additionally, the details of each layer (i.e. activations and learnables) are given in Table 1.
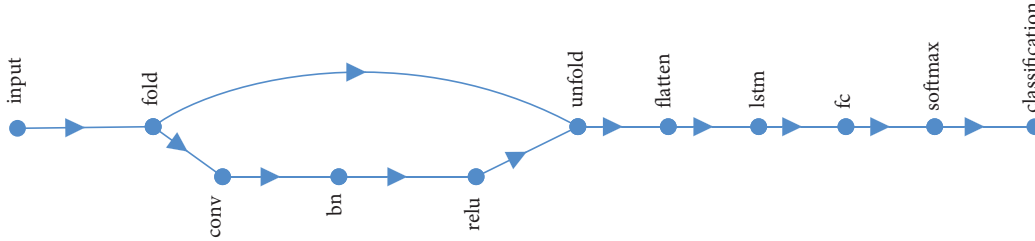

Figure 7. Layer connections of CNN-LSTM network given in Figure 6.

6. Applications and results

The methods described in detail at previous sections are implemented by using MATLAB 2019b. For both multilayer spheres, and aircraft target sets two generic CNN models, which are initially trained with dielectric (CNN$_{\text{diel.}}$) and magnetic (CNN$_{\text{mag.}}$) single layer spheres individually, are used. The model parameters, such as sphere radii and ϵ_r, are chosen to be compatible with earlier well-established strategies [i.e. MUSIC, ESPRIT, Wigner–Ville, and min-norm and waveform classification (WFC)] to compare the performance [13, 22]. The performance is measured and analyzed by accuracy ($CC = TP/(TP + FP + FN)$), sensitivity ($SE = TN/(TN + FP)$), and specificity ($SP = (TP/(TP + FP))$), where TP, TN, FP, and FN correspond to true and false positive/negative counts, respectively. The training and testing procedures are implemented using the k-fold cross-validation method, which is described below. Test sets used in k-fold are chosen to be completely different from the training sets (i.e. not used in training). The accuracy, sensitivity, and specificity values are determined for each fold, and the mean values for each of these performance metrics is obtained by averaging all results at the end of the process. Table 2 presents the description and characteristics of the target sets followed by associated quantitative information and the applied methods for each one.

For multilayer sphere classification tests, which have LARSESs at 37 aspect angles resulting in 148 signals, 21-fold cross-validation is utilized. Twenty folds (140 signals) are used for TL at Stage 2, and the remaining fold (8 signals) is used for the test. After repeating the process 20 times, the average results show that the multilayered target can be classified with 99% accuracy by both models (CNN$_{\text{diel.}}$ and CNN$_{\text{mag.}}$) proving that the deep models trained with synthetic data can converge and perform reasonably well even when the small sample size is compensated adequately with TL and data augmentation.

For aircraft model classification tests, measurements were performed for 19 aspect angles resulting in 57 signals having 14 dB SNR on average. Due to the limited number of samples, 19-fold cross-validation is used. Eighteen folds (54 signals) are used for TL at Stage 2, and the remaining fold (3 signals) is used for the test. The procedure continues until each fold is tested. The average results are presented in Table 3 after repeating the process 20 times.

As shown in Table 3, the use of magnetic spheres through CNN$_{\text{mag.}}$ has achieved the best results compared to other algorithms. Considering the relatively poor performance of CNN$_{\text{diel.}}$ model, which is significantly lower

Table 2. Details of the target data sets, utilized models and training strategies.

Target set	Relative permittivity	Relative permeability	All data (Number of signals)	Training set (Number of signals)	Test set (Number of signals)	Applied method
Magnetic single layer spheres (target set 1)	1	$\mu_{r_1} = 100$ $\mu_{r_2} = 200$ $\mu_{r_3} = 300$	1800	1600	200	CNN from scratch (stage 1)
Dielectric single layer spheres (target set 1)	$\epsilon_{r_1} = 2$ $\epsilon_{r_2} = 3$ $\epsilon_{r_3} = 4$	1	1800	1600	200	CNN from scratch (stage 1)
Magnetic multilayer spheres (target set 2)	1	$(\mu_{r_1,inner} = 100$ $\mu_{r_2,outer} = 200)$ $(\mu_{r_1,inner} = 200$ $\mu_{r_2,outer} = 100)$	74	70	4	TL with 21-fold cross-validation (stage 2)
Dielectric multilayer spheres (target set 2)	$(\epsilon_{r_1,inner} = 2$ $\epsilon_{r_2,outer} = 4)$ $(\epsilon_{r_1,inner} = 4$ $\epsilon_{r_2,outer} = 2)$	1	74	70	4	TL with 21-fold cross-validation (stage 2)
Small scale airplane models (target set 3)	Unknown (Real targets)	Unknown (Real targets)	57	54	3	TL (19-fold cross-validation - stage 2) proposed CNN-LSTM (19-fold cross-val.)

Table 3. Classification results (%) of measured scattered signals.

Target models	Boeing 747			DC 10			Boeing 767		
	CC	SE	SP	CC	SE	SP	CC	SE	SP
ESPRIT	88.2	88.5	90.9	90.6	91.4	93.5	89.9	92.4	95.5
Wigner–Wille	86.4	87.8	92.1	91.2	91.7	92.2	90.2	88.9	93.7
Min-norm	88.1	88.7	91.3	91.4	90.3	90.6	92.2	90.9	92.6
MUSIC	89.1	88.9	91.6	92.3	92.5	94.1	91.0	93.1	96.9
WFC [4]	93.3	91.1	94.4	93.3	87.8	96.1	94.1	92.2	95.0
$CNN_{diel.}$	66.6	80.1	87.7	74.5	84.0	90.3	74.3	84.9	90.0
$CNN_{mag.}$	79.7	88.4	94.5	94.6	97.1	98.5	95.5	97.6	98.8
CNN-TL [22]	94.9	98.5	98.1	98.6	99.3	99.2	97.9	99.5	99.5
$CNN\text{-}LSTM_{Raw}$	50.8	31.6	48.2	55.2	42.1	56.1	65.8	57.9	48.2
$CNN\text{-}LSTM_{Scaled}$	50.9	31.5	49.2	57.0	47.2	48.3	64.4	52.6	42.3
$CNN\text{-}LSTM_{FT}$	97.4	94.7	98.2	99.2	99.5	99.4	96.8	95.7	98.5

than the existing methods, $CNN_{mag.}$ contributes much more information to the learning process. These results also show that the adaptation to real target via TL can generate individual models having high performance if magnetic properties are utilized.

Based on these results, the use of ensembles, which would combine the outcomes of $CNN_{diel.}$ and $CNN_{mag.}$, are considered and applied. However, the initial results show that the simple fusion of these models does not

significantly improve the overall performance. Thus, a detailed analysis of the models with diversity metrics and ensemble learning strategies are needed.

For aircraft target sets, three types [trained with i) raw, ii) scaled, and iii) FT data] of CNN-LSTM models are used. Scaling and application of FT are used as preprocessing steps for CNN-LSTM$_{\text{Scaled}}$ and CNN-LSTM$_{\text{FT}}$ models, respectively. The scaling process is utilized by multiplying each signal with 10^4. On the other hand, in CNN-LSTM$_{\text{FT}}$ model, the absolute values of FT results of LARSESs are processed instead of using the only real or imaginary part of FT.

Measurements for aircraft model classification were performed for 19 aspect angles resulting in 57 signals having 14 dB SNR on average. Due to the limited number of samples, 19-fold cross-validation is utilized for all types of CNN-LSTM applications. Eighteen folds (54 signals) are used for training of the model, and the remaining fold (3 signals) is used for the test. The procedure continues until each fold is tested.

The average results are presented in Table 3 after the repetition of the folding process with the network, which has given properties, 20 times.

As shown in Table 3 and Figure 8, the use of FT as a preprocessing method through CNN-LSTM$_{\text{FT}}$ has achieved the best results compared to other algorithms. Notably, it has outperformed the recent state-of-the-art performance of [22]. Considering the relatively poor performances of CNN-LSTM$_{\text{Raw}}$ and CNN-LSTM$_{\text{Scaled}}$ models, which are significantly lower than all the methods, CNN-LSTM$_{\text{FT}}$ contributes much more information to the learning process. These results also show that even the small amount of data, CNN-LSTM model with useful features, can achieve high performance.
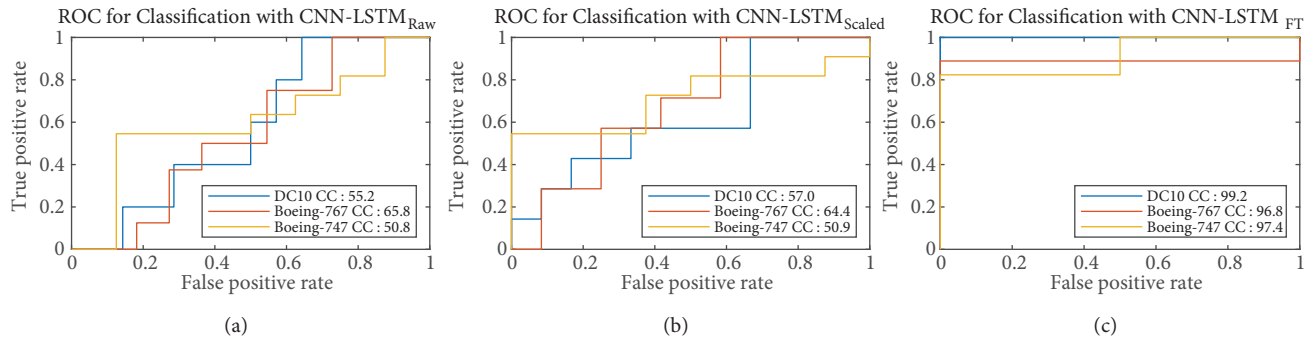

Figure 8. ROC curves for (a) CNN-LSTM$_{\text{Raw}}$, (b) CNN-LSTM$_{\text{Scaled}}$, and (c) CNN-LSTM$_{\text{FT}}$.

7. Conclusion

This study presents two main contributions to the field of target classification. First, the use of LARSESs obtained from magnetic spheres for target classification for the first time in literature. The results show that magnetic spheres can resemble the waveform structures, features, and variations characterizing complex targets (i.e. multilayer spheres and aircraft models) more effectively compared to the dielectric ones. CNNs, which intrinsically and hierarchically extract both low and high-level features through its layers, are used. These generic CNNs, which are initially trained with synthetic LARSESs data, are adapted to the actual target domain via TL. Augmentation is used to compensate for the small sample size of the measured data. The fine-tuning step is shown to be more impactful when magnetic spheres are used. This outcome shows the importance of LARSESs from magnetic objects on obtaining improved classification performance. This initial study with

multilayer magnetic spheres shows that research on increasing the accuracy in case of multiple targets and very low SNR conditions are promising future topics.

Although improved target classification performance can be achieved by the abovementioned strategy, the requirement of multiple model usage has certain drawbacks such as the creation of a base target set resembling the actual target characteristics, a significant amount of additional training data to prevent peeking of an ensemble, and excessive computational power to provide real time operation. Hence, as a second contribution, a CNN-LSTM based target classification system is proposed. The advantages of the system can be summarized as obtaining high mean accuracy even in the case of a small amount of measured scattered data and less operational costs. On the other hand, as an unavoidable drawback, the deviation from the mean accuracy affects the sensitivity and the specificity of the system performance.

References

[1] Kuznetsov AI, Miroshnichenko AE, Brongersma ML, Kivshar YS, Luk'yanchuk B. Optically resonant dielectric nanostructures. Science 2016; 354 (6314): 2472. doi: 10.1126/science.aag2472

[2] Jahani S, Jacob Z. All-dielectric metamaterials. Nature Nanotechnology 2016; 11 (1): 23-36. doi: 10.1038/nnano.2015.304

[3] Tribelsky MI, Geffrin JM, Litman A, Eyraud C, Moreno F. Small dielectric spheres with high refractive index as new multifunctional elements for optical devices. Scientific Reports 2015; 5 (1): 1-7. doi: 10.1038/srep12288

[4] Selver MA, Taygur MM, Seçmen M, Zoral EY. Hierarchical reconstruction and structural waveform analysis for target classification. IEEE Transactions on Antennas and Propagation 2016; 64 (7): 3120-3129. doi: 10.1109/TAP.2016.2567438

[5] Lannebère S, Silveirinha MG. Optical meta-atom for localization of light with quantized energy. Nature Communications 2015; 6 (1): 1-7. doi: 10.1038/ncomms9766

[6] Shore RA. Scattering of an electromagnetic linearly polarized plane wave by a multilayered sphere: obtaining a computational form of mie coefficients for the scattered field. IEEE Antennas and Propagation Magazine 2015; 57 (6): 69-116. doi: 10.1109/MAP.2015.2453885

[7] Kavur AE, Gezer NS, Barış M, Şahin Y, Özkan S et al. Comparison of semi-automatic and deep learning-based automatic methods for liver segmentation in living liver transplant donors. Diagnostic and Interventional Radiology 2020; 26 (1): 11-21. doi: 10.5152/dir.2019.19025

[8] Selver MA. A robotic system for warped stitching based compressive strength prediction of marbles. IEEE Transactions on Industrial Informatics 2019; 16 (11): 6796-6805. doi: 10.1109/TII.2019.2926372

[9] Toprak T, Belenlioğlu B, Aydın B, Güzeliş C, Selver MA. Conditional weighted ensemble of transferred models for camera based onboard pedestrian detection in railway driver support systems. IEEE Transactions on Vehicular Technology 2020; 69 (5): 5041 - 5054. doi: 10.1109/TVT.2020.2983825

[10] Dollar P, Wojek C, Schiele B, Perona P. Pedestrian detection: a benchmark. In: IEEE Conference on Computer Vision and Pattern Recognition; Miami, FL, USA; 2009. pp. 304-311.

[11] Benenson R, Omran M, Hosang J, Schiele B. Ten years of pedestrian detection, what have we learned?. In: European Conference on Computer Vision; Zurich, Switzerland; 2014. pp. 613-627.

[12] Yu D, Deng L. Deep learning and its applications to signal and information processing. IEEE Signal Processing Magazine 2011; 28 (1): 145 - 154. doi: 10.1109/MSP.2010.939038

[13] Selver MA, Seçmen M, Zoral EY. Comparison of scattered signal waveform recovery techniques under low SNR for target identification. In: IEEE 2017 11th European Conference on Antennas and Propagation; Paris, France; 2017. pp. 1091-1095.

[14] Yazdani M, Mautz J, Murphy L, Arvas E. High-frequency scattering from radially uniaxial dielectric sphere. IEEE Antennas and Wireless Propagation Letters 2015; 14: 1577-1581. doi: 10.1109/LAWP.2015.2413399

[15] Bilgin EE, Yapar A. Electromagnetic scattering by radially inhomogeneous dielectric spheres. IEEE Transactions on Antennas and Propagation 2015; 63 (6): 2677-2685. doi: 10.1109/TAP.2015.2415856

[16] Zouros GP, Kokkorakis GC. Electromagnetic scattering by a general rotationally symmetric inhomogeneous anisotropic sphere. IEEE Transactions on Microwave Theory and Techniques 2015; 63 (10): 3054-3065. doi: 10.1109/TMTT.2015.2472399

[17] Chen S, Tao C. PolSAR Image classification using polarimetric- feature-driven deep convolutional neural network. IEEE Geoscience and Remote Sensing Letters 2018; 15 (4): 627-631. doi: 10.1109/LGRS.2018.2799877

[18] Wagner SA. SAR ATR by a combination of convolutional neural network and support vector machines. IEEE Transactions on Aerospace and Electronic Systems 2016; 52 (6): 2861-2872. doi: 10.1109/TAES.2016.160061

[19] AlHajri MI, Ali NT, Shubair RM. Classification of indoor environments for iot applications: a machine learning approach. IEEE Antennas and Wireless Propagation Letters 2018; 17 (12): 2164-2168. doi: 10.1109/LAWP.2018.2869548

[20] Kavur AE, Kuncheva LI, Selver MA. Basic Ensembles of Vanilla-Style Deep Learning Models Improve Liver Segmentation From CT Images. arXiv preprint 2020; arXiv:2001.09647.

[21] Chen WC, Shuley NVZ. Robust target identification using a modified generalized likelihood ratio test. IEEE Transactions on Antennas and Propagation 2013; 62 (1): 264-273. doi: 10.1109/TAP.2013.2287019

[22] Selver MA, Toprak T, Seçmen M, Zoral EY. Transferring synthetic elementary learning tasks to classification of complex targets. IEEE Antennas and Wireless Propagation Letters 2019; 18 (11): 2267-2271. doi: 10.1109/LAWP.2019.2930602

[23] Jithesh V, Sagayaraj MJ, Srinivasa KG. LSTM recurrent neural networks for high resolution range profile based radar target classification. In: 3rd International Conference on Computational Intelligence and Communication Technology; Ghaziabad, India; 2017. pp. 1-6.

[24] Sehgal B, Shekhawat HS, Jana SK. Automatic target recognition using recurrent neural networks. In: International Conference on Range Technology; Balasore, OR, India; 2019. pp. 1-5.

[25] Zhang F, Hu C, Yin Q, Li W, Li HC et al. Multi-aspect-aware bidirectional LSTM networks for synthetic aperture radar target recognition. IEEE Access 2017; 5: 26880-26891. doi: 10.1109/ACCESS.2017.2773363

[26] Balanis CA. Advanced Engineering Electromagnetics. 2nd edition. New York, NY, USA: John Wiley & Sons, 2012.

[27] Zhang X, Geng Y, Cheng Z. A multiple-reflection solution to electromagnetic scattering by a buried sphere. IEEE Transactions on Antennas and Propagation 2020; 68 (4): 3313-3317. doi: 10.1109/TAP.2020.2971620

[28] Gholami R, Okhmatovski V. Surface-volume-surface efie formulation for fast direct solution of scattering problem on General 3-D Composite Metal-Dielectric Objects. IEEE Transactions on Antennas and Propagation 2020; 68 (7): 5742-5747. doi: 10.1109/TAP.2020.2968762

[29] Ince T, Kiranyaz S, Gabbouj M. A generic and robust system for automated patient-specific classification of ECG Signals. IEEE Transactions on Biomedical Engineering 2009; 56 (5): 1415-1426. doi: 10.1109/TBME.2009.2013934.

[30] Wu J. Target classification and identification techniques for advanced metric wave radar. In: Wu J (editor). Advanced Metric Wave Radar. 1st ed. Singapore: Springer, 2020, pp. 255-294.